Synthesis and Crystal Structure Characterization of Silicate Apatite $Sr_2Y_8(SiO_4)_6O_2$

Yiqiang Shen, Alfred Tok, and Zhili Dong [†]

School of Materials Science and Engineering,
Nanyang Technological University, Singapore 639798
[†]*Author to whom correspondence should be addressed. e-mail: zldong@ntu.edu.sg*

Pure $Sr_2Y_8(SiO_4)_6O_2$ powders were obtained after a solid-state reaction at 1400 °C for 6 h using the nanosized Y_2O_3, commercial $SrCO_3$, and silica gel. The nanosized Y_2O_3 powder was synthesized by a precipitation method using $Y(NO_3)_3$ and NH_4HCO_3, followed by a heat treatment. The crystal structure of $Sr_2Y_8(SiO_4)_6O_2$ was characterized by powder X-ray diffraction, Rietveld refinement, and high-resolution transmission electron microscopy. Results show that $Sr_2Y_8(SiO_4)_6O_2$ has a typical apatite-type structure $A^I_4A^{II}_6(BO_4)_6X_2$ in the *P*6$_3$/*m* space group. The lattice parameters are *a* = 9.3884(6) Å and *c* = 6.8657(4) Å. There are two special sites, A^I (4f) and A^{II} (6h), in the apatite structure. The A^{II} sites are fully occupied by Y, while the A^I sites are randomly filled by Y and Sr atoms. The crystallographic data obtained from $Sr_2Y_8(SiO_4)_6O_2$ and other silicate oxyapatites are compared and summarized.

I. Introduction

Natural and synthetic apatite-type materials have been widely investigated in many fields such as catalysis,[1] environmental remediation,[2] and bone engineering.[3] The general formula of an apatite-type compound is $A^I_4A^{II}_6(BO_4)_6X_2$. The A^I (Wycoff 4f site) and A^{II} (Wycoff 6h site) positions are two distinct crystallographic sites that

accommodate alkali, alkaline-earth, or rare-earth atoms, the B site is occupied by phosphorous, vanadium, silicon, boron, or germanium, and X is the anion site for halogen, hydroxyl, or oxygen. Because of the variety of the elements incorporated and the complexity of the apatite crystal structures, a large number of studies on crystal chemistry have been reported.[4–9] Most apatites belong to the space group $P6_3/m$, while variants belong to space groups with lower symmetries (e.g., $P6_3$ and $P2_1/m$).[10] The thermal stabilities of the hydroxyl-apatite, chloride-apatite, and fluoride-apatite are not very good, a property which limits their applications. However, this deficiency can be overcome by one group, the silicate oxyapatites, whose melting points are higher.[11]

The present study focuses on the synthesis and crystal structure characterization of silicate oxyapatites. A pure-phase silicate oxyapatite material, $Sr_2Y_8(SiO_4)_6O_2$ (SYS), can be obtained by a modified solid-state reaction. This apatite material is a promising candidate for the host material of solid-state laser[12–15] and phosphors.[16] Although crystal structure has a great impact on the performance of lasers and phosphors, no detailed structural data of SYS have been reported. Herein, the synthesis of SYS is reported as well as its crystal structure is studied by X-ray diffraction (XRD), Rietveld refinement, and high-resolution transmission electron microscopy (HRTEM). These data will provide a foundation for resolving more complicated crystal structures of rare-earth element-doped SYS systems with application in optics and lasers. The structure of SYS is compared with other reported silicate oxyapatites.

II. Experimental Procedure

(1) Synthesis of Nanosized Y_2O_3

Two kinds of powders NH_4HCO_3 (>99.0%, Fluka, St. Louis, MO) and $Y(NO_3)_3$ (99.9%, Aldrich, St. Louis, MO) were dissolved in deionized water to form 2.5 mol/L NH_4HCO_3 and 0.5 mol/L $Y(NO_3)_3$ solutions. Then NH_4HCO_3 was slowly added dropwise into the $Y(NO_3)_3$ solution with stirring, during which a white precipitant appeared. In order to precipitate all the yttrium, 10% excess NH_4HCO_3 was added rather than the stoichiometric amounts according to the following reaction:

$$2Y(NO_3)_3 + 6NH_4HCO_3 \rightarrow Y_2(CO_3)_3(H_2O)_2 \downarrow + 6NH_4NO_3 + H_2O + 3CO_2 \uparrow \quad (1)$$

The as-precipitated slurry was washed twice with water and twice with ethanol and centrifuged. Finally, the precipitate was dried at 70°C in an oven and calcined at a higher temperature for 4 h in a muffle furnace with a heating rate of 5°C/min. Thermal gravimetric analysis (TGA) was used to determine the calcination temperature.

(2) Synthesis of $Sr_2Y_8(SiO_4)_6O_2$

For comparison, the commercial (99.9%, Alfa Aesar, Ward Hill, MA, ~1 μm) and synthetic nanosized Y_2O_3 powders were used separately in solid-state reactions. Stoichiometric amount of $SrCO_3$ (>99.0%, Alfa Aesar), silica gel 60 (>99.0%, Fluka), and Y_2O_3 were weighted according to the formula $Sr_2Y_8(SiO_4)_6O_2$ to give a total of 4 g for each batch. The powders were mixed for 12 h by horizontal ball milling with ZrO_2 balls and ethanol, and the resultant slurry was dried at 70°C overnight in oven, followed by a solid-state reaction at 1400°C for 6 h in a muffle furnace with a heating rate of 5°C/min.

(3) Characterizations

The phase compositions of the as-synthesized samples were studied by XRD. Diffraction patterns were collected using an X-ray diffractometer (Shimadzu 6000, Kyoto, Japan) with Cu*K*α radiation. The machine was operated at 40 kV and 30 mA with a step size of 0.02° and a scan speed of 2°/min. Furthermore, Rietveld refinement was carried out using TOPAS (Version 3.0. Bruker AXS, Karlsruhe, Germany). As no structural details about SYS were known, crystallographic data from $NaY_9(SiO_4)O_2$ apatite (ICSD #27191) were used as the starting model. The parameters were refined in the following sequence: background by using Chebychev function, cell parameters, crystal size, atom positions, global thermal parameters, and site occupancies.

The morphologies as well as particle sizes of both commercial and synthetic Y_2O_3 powders were examined using a JEOL JSM6360 scanning electron microscope (SEM,

Tokyo, Japan) operating at 15 kV. The local structure of SYS was investigated using a JEOL JEM-2010 transmission electron microscope (Cs = 0.5 mm, accelerating voltage = 200 kV, Scherzer defocus ≈ -43 nm). Selected area electron diffraction patterns (SAD) and HRTEM images were collected.

(4) Comparison with the Published Crystal Structure Data

In total, 17 chemical end-members of silicate apatites with space group $P6_3/m$ were selected for the study of their structural characteristics[17–21] (Table I). Both single crystal and polycrystalline powder samples were included. As all the silicate oxyapatites selected conform to the general formula $A^{I}_4A^{II}_6(SiO_4)_6X_2$; the crystal structure variation is only due to the atoms occupying the A^{I} and A^{II} sites. Instead of considering the average ionic size for A^{I} and A^{II}, this study used the concept of the effective ionic radius separately for each of A^{I} and A^{II}. The definition is as follows:

$$r_{\text{eff}}^{A^m} = \sum_{i=1}^{n} r_i^{A^m} \times \eta_i^{A^m} \quad (m = I \text{ or II}) \qquad (2)$$

where $r_{\text{eff}}^{A^I}$ (or $r_{\text{eff}}^{A^{II}}$) is the effective ionic radius of A^{I} (or A^{II}), $r_i^{A^I}$ (or $r_i^{A^{II}}$) is the ionic radius of atom (or vacancy) i at A^{I} (or A^{II}), and $\eta_i^{A^I}$ (or $\eta_i^{A^{II}}$) is the occupancy of the atom (or vacancy) i at A^{I} (or A^{II}). As it is difficult to determine the radius of vacancies, the value is considered to be zero. This treatment is believed to underestimate the value of the vacancy's radius, because the coordinated oxygen atoms are negatively charged and the repulsion between them would prevent them from contacting. However, this treatment can simplify the calculation.

III. Results and Discussion

(1) Characterization of the Synthetic Y_2O_3

XRD analysis of the precipitates obtained by the chemical reaction between NH_4HCO_3 and $Y(NO_3)_3$ (Fig. 1) shows that the main phase is $Y_2(CO_3)_3(H_2O)_2$, which is in good agreement with Eq. (1).

TG–DTA results of the precipitates are shown in Fig. 2. According to the TG curve, a continuous decrease of the sample weight occurs with increasing temperature with the process ceasing at about 620°C. In the DTA profile, the two endothermic peaks below 150°C are related to the dehydration of $Y_2(CO_3)_3(H_2O)_2$ ($Y_2(CO_3)_3(H_2O)_2 \rightarrow Y_2(CO_3)_3+2H_2O\uparrow$) and the decomposition of the residual ammonium species, respectively; the endothermic peak at about 340°C corresponds to the further decomposition of the precipitate ($Y_2(CO_3)_3 \rightarrow Y_2O_3+CO_2\uparrow$). This decomposition process was completed only when the temperature reached 620°C, consistent with the TG profile. The last endothermic peak at about 620°C is due to the crystallization of the Y_2O_3 from the amorphous materials, which explains why the precipitates calcined at 500°C are not well crystallized compared with those calcined at 700°C as discussed in the following.

The precipitates were calcined at 500°, 700°, and 900°C. The XRD results of these samples are shown in Fig. 3. At the calcination temperature of 500°C, $Y_2(CO_3)_3(H_2O)_2$ decomposed and the Y_2O_3 phase appeared. The XRD peaks of the Y_2O_3 phase are broad and weak, indicating that the precipitates are poorly crystalline not well crystallized and the amorphous materials are still present. The precipitates are crystalline after 700°C calcination and the peaks of Y_2O_3 in the XRD pattern sharpen. Thus, for subsequent experiments, Y_2O_3 calcined at 700°C was used. For 900°C calcined samples, the higher temperature results in larger crystal size and the peaks in the XRD pattern are narrower.

SEM images of commercial and synthetic nanosized Y_2O_3 powders are shown in Fig. 4. From these, it is evident that the synthetic Y_2O_3 powders are much smaller (80–100 nm) and more homogenous than the commercial powders. Moreover, the particles are well dispersed as the loose agglomerates shown in the figures can be broken down easily. The well-defined nature of the synthetic powders results in high reactivity in solid-state reactions.

(2) Purity of the As-Synthesized $Sr_2Y_8(SiO_4)_6O_2$

XRD patterns from samples obtained by solid-state reactions using synthetic and commercial Y_2O_3 powders were compared (Fig. 5). Several extra peaks existed in the XRD pattern when commercial Y_2O_3 was used and some of them were indexed as coming from Y_2O_3 and SiO_2 due to incomplete reaction. As the starting materials were mixed stoichiometrically, residual strontium compounds were expected to exist as well although they were not observed in the XRD pattern. There are two possible explanations for this: one is that the amount of the strontium compounds left is relatively low and can not be identified by XRD; the other is that the XRD peaks of strontium compounds are overlapped with those of the SYS apatite. However, when synthetic Y_2O_3 was used, no impurity phases were detected by XRD, indicating that the synthetic Y_2O_3 powders were uniformly mixed with other starting materials and reacted very effectively during the heating process.

(3) Crystal Structure of $Sr_2Y_8(SiO_4)_6O_2$

Rietveld refinement also suggested the formation of pure apatite phase in the sample when using synthetic Y_2O_3 as all the experimental XRD peaks were well fitted by the calculated data, as given in Fig. 6. The space group of SYS was confirmed to be $P6_3/m$, because when other space groups instead of $P6_3/m$ model were used, the calculation of the Rietveld refinement was diverged. In order to investigate the Sr and Y distribution among the A^{I} (4f) and A^{II} (6*h*) sites, site occupancies at A^{I} and A^{II} sites were refined with some constraints. Supposing occupancy of Y in A^{II} site is *x*, and the rest of Y occupy A^{I} site, then the occupancy of Y in A^{I} site is $2–1.5x$. The multiplicity for A^{I} and A^{II} are 4 and 6, respectively; therefore, the occupancies for Sr in A^{I} and A^{II} are $1.5x$-1 and 1-*x*. The refined data (Table II) show that A^{II} sites are fully occupied by Y, while Sr and Y are randomly distributed in A^{I} sites, which agrees with F. Druon's results.[22] The order–disordered structure is desired for ultrafast laser host materials.[13]

Polyhedral description of the apatite crystal is based on the Rietveld refinement results. Three kinds of polyhedra, Si–O tetrahedra, A^{I}–O and A^{II}–O polyhedra, are

shown in the structure (Fig. 7). The bond lengths of Si–O in the Si–O tetrahedra range from 1.577(16) to 1.607(7) Å with the mean value of 1.598(4) Å. The bond angles of O–Si–O in the tetrahedra range from 103.7(7)° to 112.5(5)° (Table III). The bond length distortion[23] (BLD, the standard deviation of the bond length from the mean value) and the tetrahedral angle variance[24] (TAV, the deviation of the bond angles from the ideal tetrahedra) are two criteria to measure the distortion of the tetrahedra quantitatively. In the present case, the BLD for the Si–O is 0.77(2)% and the TAV is 10.9(8). The Si–O tetrahedra are more distorted compared with the P–O tetrahedral in $Ca_5(PO_4)_6F$[25] as the BLD and TAV values of the latter are 0.20(5)% and 3.4(2), respectively. A possible reason is that smaller ionic-sized phosphorous may feel more comfortable in the P–O tetrahedra. The distorted Si–O polyhedra are a common feature in many other silicate oxyapatites as discussed by Redhammer and Roth.[18] Si–O tetrahedra are isolated from each other but have an important function to connect the A^I–O and A^{II}–O polyhedra. There are four A^I–O polyhedra around one Si–O tetrahedron (Fig. 7(b)). Two of the A^I–O polyhedra and the Si–O tetrahedron share an O1 atom. The other two A^I–O polyhedra are connected with the Si–O tetrahedron via their O2–O3 edges, and the O2 atom is the common point of the three polyhedra. The Si–O tetrahedron is also surrounded by five A^{II}–O polyhedra (Fig. 7(d)). Four of the A^{II}–O polyhedra are separately connected with the Si–O tetrahedron by vertex-sharing, and the other A^{II}–O polyhedron connects the Si–O tetrahedron via O3–O3 edge sharing.

For the A^I–O polyhedra, the centered A^I site has a local symmetry of C_3 and the nine coordinated oxygen atoms form a tricapped trigonal-prismatic geometry (Figs. 7(a) and (b)). The A^I–O bonds consist of three A^I–O1 and three A^I–O2 which are 2.375(11) and 2.489(17) Å in length, respectively, and three longer A^I–O3 bonds with 2.815(10) Å (Table III). Two trigonal prisms, A^IO1_3 and A^IO2_3, are formed by the corresponding ions in one A^I–O polyhedron. These two trigonal prisms have a common vertex at the A^I position, and have two parallel triangle bases that are normal to the *c*-axis and defined by the O1 and the O2 atoms. These two prisms are twisted with respect to each other as viewed from the *c*-axis. The twist angle φ (Fig. 7(a)) is actually the projection of the bond angle O1–A^I–O2 at the (0001) plane and it is proved to be a

quantitative parameter to measure the deviations of the apatite-type compounds from regular anion nets.[10] The twist angle in the A^I–O polyhedra of SYS is 25.04°, which is larger than that of the $Ca_5(PO_4)_6F$ (φ = 23.3°).[10] Two neighboring A^I–O polyhedra share faces composed by either three O1 or three O2 atoms along the *c*-axis, forming A^I–O polyhedra columns. Six such columns surround the centered O4 atom. The columns are isolated from each other and connected by Si–O tetrahedra (Fig. 7(b)).

The A^{II} site is coordinated by seven oxygen atoms, one O1, one O2, four O3, and one O4. The bond lengths of A^{II}–O range from 2.2014(5) to 2.659(11) Å and result in irregular polyhedra with pentagonal bipyramidal geometry (Figs. 7(c) and (d)). One interesting point in these polyhedra is the O4 atom. It resides at position 2*a* ($x = y = 0$, $z = 1/4$) and is triangularly surrounded by three Y atoms at A^{II} site with $z = 1/4$. The O4 atom does not belong to any Si–O tetrahedra and the sum of the bond valence of the surrounded cations towards O4 is considerably <2 (~1.8 in the current case). This under-bounded oxygen atom has a significant influence on not only the trend of the cation occupancy but also the luminescent properties.[26] Moreover, in the fluoride-apatites like $Ca_5(PO_4)_6F$, the O4 atom is replaced by F atom but lies the same position. However, for the substation of a larger anion such as Cl^- (for C.N. = 6, the ionic radius $r_{Cl}^- = 1.81$, $r_O^{2-} = 1.40$, and $r_F^- = 1.33$ Å), the anion will enter 2b ($x = y = z = 0$) instead, because the 2b site provides larger space for the big anions.[27]

An HRTEM image and the corresponding SAD along $[2\bar{1}10]$ zone axis are shown in Fig. 8. The *d*-spacing values of the $(01\bar{1}0)$ planes and the (0001) planes are about 8.1 and 6.9 Å, respectively. According to the hexagonal crystallographic features, the *d*-spacing values of these two sets of planes can be calculated from the lattice parameters obtained from the XRD refinement (Table I):

$$d_{(01\bar{1}0)} = a \times \cos 30^\circ = 9.3384 \times \frac{\sqrt{3}}{2}\,\text{Å} = 8.0873 \approx 8.1\,\text{Å}$$
$$d_{(0001)} = c = 6.8657 \approx 6.9\,\text{Å} \qquad (3)$$

The consistency between the XRD refinement and the HRTEM results clearly indicates that the as-synthesized product is $Sr_2Y_8(SiO_4)_6O_2$ apatite.

(4) Crystal Structures of the Silicate Oxyapatites

The relationship between the lattice parameters (*a* and *c*) and the $r_{\text{eff}}^{A^I}$ (or $r_{\text{eff}}^{A^{II}}$) are shown in Fig. 9. Data points are divided into four groups: $Sr_2RE_8(SiO_4)_6O_2$, $NaRE_9(SiO_4)_6O_2$, $LiRE_9(SiO_4)_6O_2$, and $RE_{9.33}(SiO_4)_6O_2$. With respect to each group, the lattice parameters increase almost linearly with the increase of the effective ionic radius of A^I. Small deviations from the linear fittings exist because different samples (single crystal or powder) and characterization techniques (X-ray or neutron diffraction) were used in the literatures (Table IV). Based on the data for $NaRE_9(SiO_4)_6O_2$ and $LiRE_9(SiO_4)_6O_2$) apatites as shown in (Figs. 9(a) and (b)), a larger RE cation is needed for $LiRE_9(SiO_4)_6O_2$ in order to reach the similar $r_{\text{eff}}^{A^I}$ value as $NaRE_9(SiO_4)_6O_2$. It is believed that this larger RE at A^I position expands the unit cell effectively, resulting in increase of the lattice constants *a* and *c*. The data for $Sm_{10}(SiO_4)_6O_2$ follow the trends for the $Sr_2RE_8(SiO_4)_6O_2$ group. This can be explained by the similar ionic radius of Sm^{2+} and Sr^{2+} (r_{Sm}^{2+} = 1.19 Å, r_{Sr}^{2+} = 1.18 Å). $Sm_{10}(SiO_4)_6O_2$ can be expressed as $Sm^{2+}Sm_8^{3+}(SiO_4)_6O_2$ because of the coexistence of Sm^{2+} and Sm^{3+}.[21]

As almost all the alkali or alkaline-earth atoms have entered the A^I site, the average ionic radius at A^{II} only represents the trivalent rare-earth atoms. Therefore, from Figs. 9(b) and (c), the relationships between the unit cell constraints and $r_{\text{eff}}^{A^{II}}$ do not obviously depend on the alkali or alkaline-earth atoms.

IV. Conclusion

Homogeneous nanosized Y_2O_3 powders have been obtained from the precipitation method. The good sinterability of the synthetic Y_2O_3 powders helps to produce pure $Sr_2Y_8(SiO_4)_6O_2$ powder materials by a solid-state reaction. $Sr_2Y_8(SiO_4)_6O_2$ has a typical apatite-type structure with the $P6_3/m$ space group. The lattice constants *a* = 9.3884(6)Å and *c* = 6.8657(4) Å. The A^{II} (6h) sites are fully occupied by Y while the A^I (4f) sites

are randomly filled by Y and Sr. Fundamental crystallographic features can be elucidated through Si–O, A^{I}—O, and A^{II}–O polyhedral networks. Lattice parameters of silicate oxyapatites are highly dependent on the different cations occupied at A^{I}, and it is able to distinguish these cations by using the concept of effective ionic radius of A^{I} or A^{II}.

Acknowledgment

The authors would like to thank Prof. Edward R. T. Tiekink for his critical comments on the manuscript.

References

[1]B. M. Choudary, C. Sridhar, M. L. Kantam, G. T. Venkanna, and B. Sreedhar, "Design and Evolution of Copper Apatite Catalysts for *N*-Arylation of Heterocycles with Chloro- and Fluoroarenes," *J. Am. Chem. Soc.*, **127** [28] 9948–9 (2005).

[2]X. B. Chen, J. V. Wright, J. L. Conca, and L. M. Peurrung, "Effects of pH on Heavy Metal Sorption on Mineral Apatite," *Environ. Sci. Technol.*, **31** [3] 624–31 (1997).

[3]L. L. Hench, "Bioceramics—From Concept to Clinie," *J. Am. Ceram. Soc*., **74** [7] 1487–510 (1991).

[4]J. Felsche, *Structure and Bonding*. Berlin, Springer, 1973.

[5]D. E. C. Corbridge, *The structural Chemistry of Phosphorus*. Elsevier, Amsterdam, 1974.

[6]P. H. J. Mercier, Y. Le Page, P. S. Whitfield, and L. D. Mitchell, "Geometrical Parameterization of the Crystal Chemistry of $P6_3/m$ Apatite. II. Precision, Accuracy and Numerical Stability of the Crystal-Chemical Rietveld Refinement," *J. Appl. Crystallogr.*, **39**, 369–75 (2006).

[7]J. Y. Kim, Z. L. Dong, and T. J. White, "Model Apatite Systems for the Stabilization of Toxic Metals: II, Cation and Metalloid Substitutions in Chlorapatites," *J. Am. Ceram. Soc.*, **88** [5] 1253–60 (2005).

[8]M. I. Kay, R. A. Young, and A. S. Posner, "Crystal Structure of Hydroxyapatite," *Nature*, **204** [496] 1050–2 (1964).

[9]Z. L. Dong, T. J. White, B. Wei, and K. Laursen, "Model Apatite Systems for the Stabilization of Toxic Metals: I, Calcium Lead Vanadate," *J. Am. Ceram. Soc.*, **85** [10] 2515–22 (2002).

[10]T. J. White and Z. L. Dong, "Structural Derivation and Crystal Chemistry of Apatites," *Acta Crystallogr., Sect. B: Struct. Sci.*, **59**, 1–16 (2003).

[11]Kb. Steinbru, G. W. Roland, N. T. Melamed, R. Mazelsky, E. P. Riedel, R. H. Hopkins, and T. Hennings, "Laser Properties of Nd^{3+} and Ho^{3+} Doped Crystals with Apatite Structure," *Appl. Opt.*, **11** [5] 999–1012 (1972).

[12]F. Druon, S. Chenais, and F. Raybaut, "Apatite-Structure Crystal, Yb^{3+}: $SrY_4(SiO_4)_3O$, for the Development of Diode-Pumped Femtosecond Lasers," *Opt. Lett.*, **27** [21] 1914–6 (2002).

[13]F. Druon, F. Balembois, and P. Georges, "Laser Crystals for the Production of Ultra-Short Laser Pulses," *Ann. Chim. Sci. Mat.*, **28**, 47–72 (2003).

[14]F. Druon, F. Balembois, and P. Georges, "Ultra-Short-Pulsed and Highly-Efficient Diodepumped Yb: SYS Mode-Locked Oscillators," *Opt. Express*, **12** [20] 5005–12 (2004).

[15]F. Druon and P. Georges, "Pulse-Compression Down to 20 fs Using a Photonic Crystal Fiber Seeded by a Diode-Pumped Yb: SYS Laser at 1070 nm," *Opt. Express*, **12** [15] 3383–96 (2004).

[16]T. J. Isaacs, "Study of Eu^{3+} Fluorescence in Some Silicate Oxyapatites," *J. Electrochem. Soc.*, **120** [5] 654–6 (1973).

[17]J. Felsche, "Rare-Earth Silicate with Apatite Structure," *J. Solid State Chem.*, **5** [2] 266–75 (1972).

[18]G. R. Redhammer and G. Roth, "Lithium and Sodium Yttrium Orthosilicate Oxyapatite, $LiY_9(SiO_4)_6O_2$ and $NaY_9(SiO_4)_6O_2$, at Both 100 K and Near Room Temperature," *Acta Crystallogr., Sect. C: Cryst.*, **59**, 1120–4 (2003).

[19]Y. Masubuchi, M. Higuchi, T. Takeda, and S. Kikkawa, "Oxide Ion Conduction Mechanism in $RE_{9.33}(SiO_4)_6O_2$ and $Sr_2RE_8(SiO_4)_6O_2$ (RE = La, Nd) from Neutron Powder Diffraction," *Solid State Ion.*, **177** [3–4] 263–8 (2006).

[20]R. P. Gunawardane, R. A. Howie, and F. P. Glasser, "Structure of the Oxyapatites $NaY_9(SiO_4)_6O_2$," *Acta Crystallogr., Sect. B: Struct. Sci.*, **38** [5] 1564–6 (1982).

[21]M. G. Morgan, M. T. Wang, and A. Mar, "Samarium Orthosilicate Oxyapatite, $Sm_5(SiO_4)_3O$," *Acta Crystallogr. Sect. E: Struct. Rep.*, **58**, 170–1 (2002).

[22]F. Druon, S. Chenais, P. Raybaut, F. Balembois, P. Georges, R. Gaume, P. H. Haumesser, B. Viana, D. Vivien, S. Dhellemmes, V. Ortiz, and C. Larat, "Apatite Structure Crystal, Yb^3: $SrY_4(SiO_4)_3O$, for the Development of Diode-Pumped Femtosecond Lasers," *Opt. Lett.*, **27** [21] 1914–6 (2002).

[23]B. Renner and G. Lehmann, "Correlation of Angular and Bond Length Distortions in TO_4 Units in Crystals," *Z. Kristall.*, **175** [1–2] 43–59 (1986).

[24]K. Robinson, G. V. Gibbs, and P. H. Ribbe, "Quadratic Elongation—Quantitative Measure of Distortion in Coordination Polyhedra," *Science*, **172** [3983] 567–70 (1971).

[25]K. Sudarsan, R. A. Young, and P. E. Mackie, "Comparison of Synthetic and Mineral Fluorapatite $Ca_5(PO_4)_3F$ in Crystallographic Detail," *Mater. Res. Bull.*, **7** [11] 1331–8 (1972).

[26]G. Blasse, "Influence of Local Charge Compensation on Site Occupation and Luminescence of Apatites," *J. Solid State Chem.*, **14** [2] 181–4 (1975).

[27]M. Bauer and W. E. Klee, "Induced Ferrielectricity in Chlorapatite," *Z. Kristall.*, **206**, 15–24 (1993).

List of Tables

List of Figures

atoms have the same *z* value (z = 1/4). (d) The connection of the Si–O tetrahedra and A^{II}–O polyhedra is shown along *a*-axis direction.

Fig.8. High-resolution transmission electron microscopic image of $Sr_2Y_8(SiO_4)_6O_2$ along $[2\bar{1}10]$ zone axis, inset is the selected area diffraction pattern.

Fig. 9. The relationship between the effective ionic radius of A^{I} and the lattice parameters *a* and *c* are shown in (a) and (b), respectively. The relationship between the effective ionic radius of A^{II} and the lattice parameters *a* and *c* are shown in (c) and (d), respectively. The resultant lines of the linear fitting within each group are also shown.

Phase name	$Sr_2Y_8(SiO_4)_6O_2$
R_{Bragg}	3.961
GOF	1.48
Space group	$P6_3/m$
Cell mass	1496.630
Cell volume (Å^3)	524.076(79)
Crystallite size (nm)	157.6
Crystal density (g/cm^3)	4.74
Lattice parameters:	
a (Å)	9.3884(6)
c (Å)	6.8657(4)
Z	1
θ range for data collection	10°–90°
Refinement method	Full-matrix least-squares on F^2

$R_{Bragg} = \frac{\sum |I_{k,obs} - I_{k,calc}|}{\sum I_{k,obs}}$ GOF $= \frac{R_{wp}}{R_{exp}} = \sqrt{\frac{\sum w_m (Y_{m,obs} - Y_{m,calc})^2}{M-P}}$ where $I_{k,obs}$ and $I_{k,calc}$ are the observed and calculated intensities of the kth reflection, respectively; R_{wp} is R-weighted pattern and R_{exp} is R-expected value; w_m is the reciprocal of the variance for each observation; $Y_{m,obs}$ and $Y_{m,calc}$ are the observed and calculated data respectively at data point m; M is the number of data points and P is the number of parameters. GOF, goodness of fit.

Table I.

Atom	Site	*x*	*y*	*z*	Occupation
Y/Sr	4f (A^{I})	1/3	2/3	0.0008 (6)	0.5/0.5
Y/Sr	6h (A^{II})	0.2324 (2)	0.9959 (4)	1/4	1/0
Si	6h	0.3958 (7)	0.3709 (7)	1/4	1
O1	6h	0.3139 (14)	0.4823 (14)	1/4	1
O2	6h	0.5925 (14)	0.4767 (14)	1/4	1
O3	12i	0.3378 (10)	0.2488 (10)	0.0659 (10)	1
O4	2a	0	0	1/4	1

Table II.

Bond lengths of A^{I} (4f)–O		Bond lengths A^{II}(6h)–O	
A^{I}–O1 × 3	2.375 (11)	A^{II}–O4	2.2014 (5)
A^{I}–O2 × 3	2.489 (17)	A^{II}–O3 × 2	2.342 (8)
A^{I}–O3 × 3	2.815 (10)	A^{II}–O2	2.378 (11)
		A^{II}–O3 × 2	2.422 (9)
Bond lengths of Si–O		Bond angles of O–Si–O	
Si–O1	1.577 (16)	O2–Si–O1	112.5 (5)
Si–O2	1.601 (13)	O2–Si–O3	108.5 (6)
Si–O3 × 2	1.607 (7)	O1–Si–O3	111.7 (6)
		O3–Si–O3	103.7 (7)

Table III.

Compound name	a (Å)	c (Å)	Occupancy of A^{I}	Occupancy of A^{II}	$r_{eff}^{A^{I}}$ (Å)	$r_{eff}^{A^{II}}$ (Å)	Reference
$LiY_9(SiO_4)_6O_2$[†]	9.3376	6.7321	Li/Y = 0.25/0.75	Y = 1	0.995	0.9	Redhammer and Roth[18]
$NaY_9(SiO_4)_6O_2$[†]	9.3386	6.7589	Na/Y = 0.25/0.75	Y = 1	1.06	0.9	
$La_{9.33}(SiO_4)_6O_2$[‡]	9.7228	7.1881	Vac/La = 0.167/0.833	La = 1	0.966	1.03	Masubuchi *et al.*[19]
$Sr_2La_8(SiO_4)_6O_2$[‡]	9.7048	7.2411	Sr/La = 0.5/0.5	La = 1	1.21	1.03	
$Nd_{9.33}(SiO_4)_6O_2$[‡]	9.569	7.0225	Vac/Na = 0.167/0.833	Nd = 1	0.932	0.98	
$Sr_2Nd_8(SiO_4)_6O_2$[‡]	9.5666	7.1062	Sr/Nd = 0.5/0.5	Nd = 1	1.19	0.98	
$NaY_9(SiO_4)_6O_2$[†]	9.334	6.759	Na/Y = 0.25/0.75	Y = 1	1.06	0.9	Gunawardane *et al.*[20]
$Sm_{10}(SiO_4)_6O_2$	9.4959	7.0361	Sm^{2+}/Sm^{3+} = 0.5/0.5	Sm^{3+} = 1	1.175	0.96	Morgan *et al.*[21]
$Dy_{9.33}(SiO_4)_6O_2$	9.373	6.784	Vac/Dy = 0.167/0.833	Dy = 1	0.858	0.91	Felsche[17]
$Gd_{9.33}(SiO_4)_6O_2$	9.401	6.825	Vac/Gd = 0.167/0.833	Gd = 1	0.874	0.94	
$Tm_{9.33}(SiO_4)_6O_2$	9.30	6.666	Vac/Tm = 0.167/0.833	Tm = 1	0.824	0.88	
$LiLa_9(SiO_4)_6O_2$	9.681	7.160	Li/La = 0.25/0.75	La = 1	1.10	1.03	
$LiNd_9(SiO_4)_6O_2$	9.529	6.994	Li/Nd = 0.25/0.75	Nd = 1	1.07	0.98	
$LiGd_9(SiO_4)_6O_2$	9.413	6.852	Li/Gd = 0.25/0.75	Gd = 1	1.018	0.94	
$NaLa_9(SiO_4)_6O_2$	9.687	7.180	Na/La = 0.25/0.75	La = 1	1.165	1.03	
$NaNd_9(SiO_4)_6O_2$	9.535	7.027	Na/Nd = 0.25/0.75	Nd = 1	1.135	0.98	
$NaGd_9(SiO_4)_6O_2$	9.419	6.878	Na/Gd = 0.25/0.75	Gd = 1	1.083	0.94	

[†]The samples are single crystals. The rest are powder form. [‡]The samples are characterized by the neutron diffraction. The rest are tested by X-ray diffraction. Vac, vacancy.

Table IV.

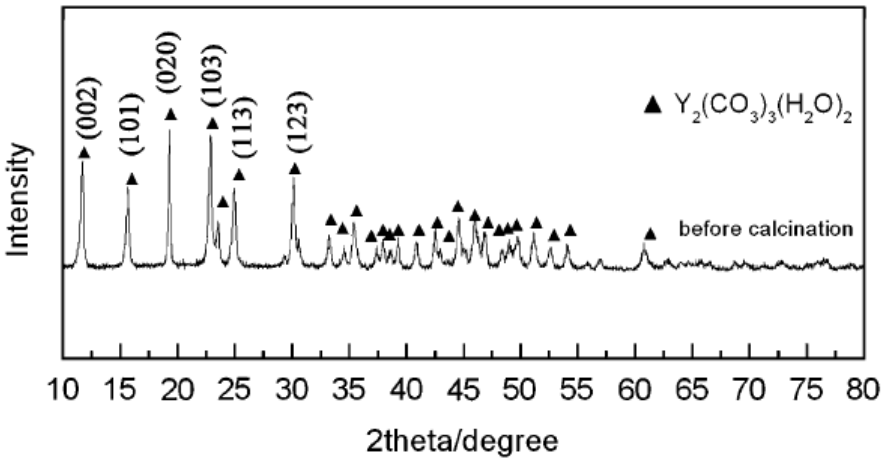
(002)
(101)
(020)
(103)
(113)
(123)
▲ $Y_2(CO_3)_3(H_2O)_2$
before calcination
Intensity
10 15 20 25 30 35 40 45 50 55 60 65 70 75 80
2theta/degree

Fig. 1

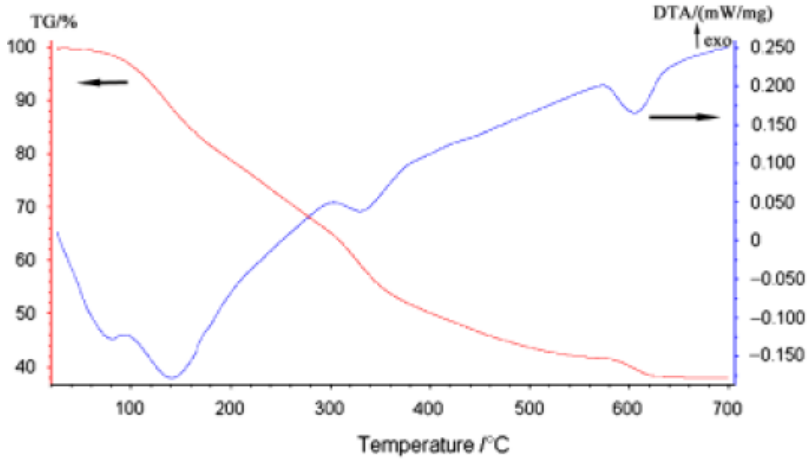
TG/%
DTA/(mW/mg)
exo
100
90
80
70
60
50
40
0.250
0.200
0.150
0.100
0.050
0
−0.050
−0.100
−0.150
100
200
300
400
500
600
700
Temperature /°C

Fig. 2

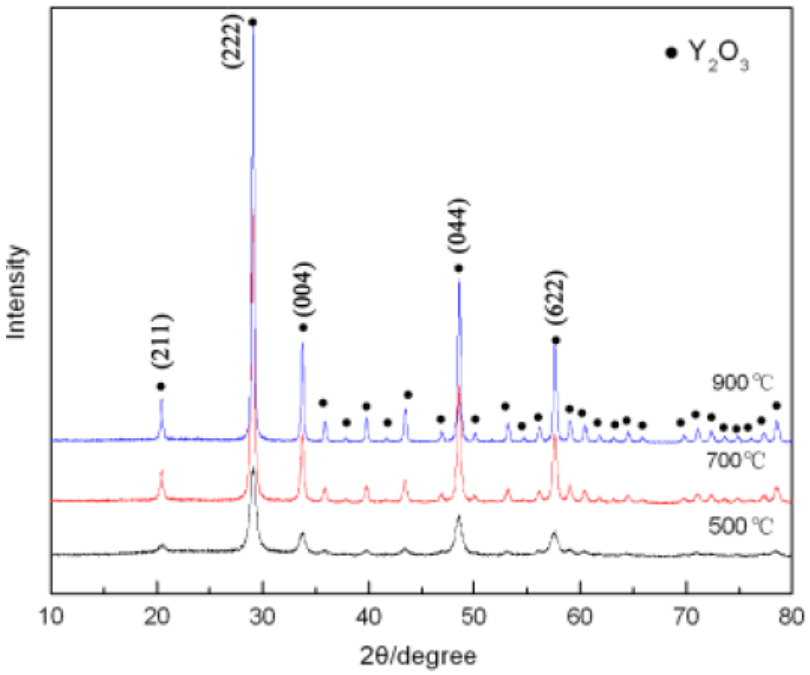
(222)
• Y_2O_3
(211)
(004)
(044)
(622)
Intensity
900℃
700℃
500℃
10
20
30
40
50
60
70
80
2θ/degree

Fig. 3

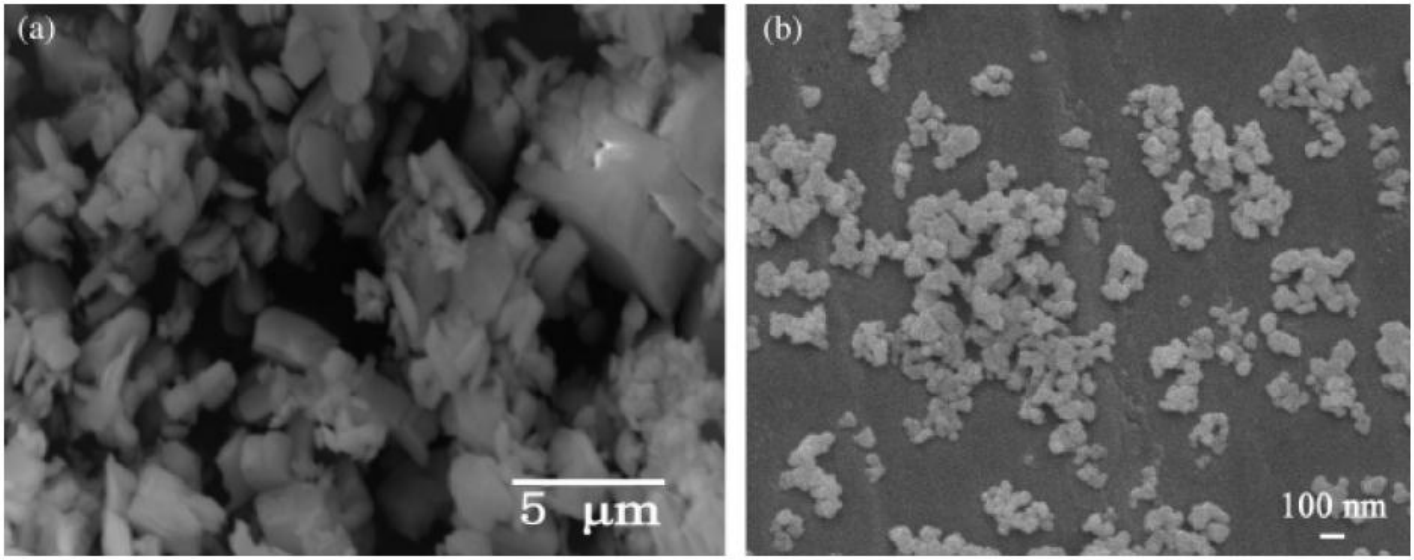

Fig. 4

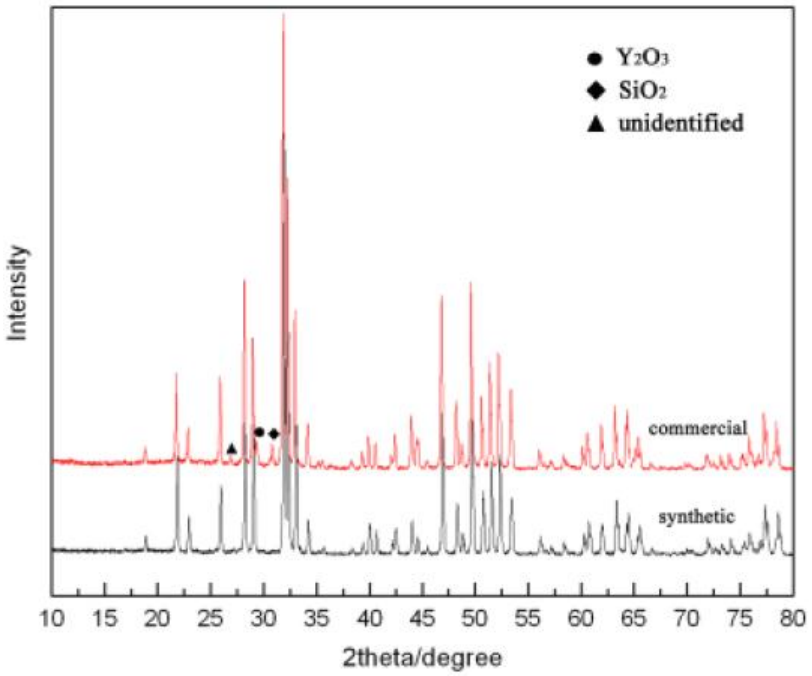
● Y2O3
◆ SiO2
▲ unidentified
Intensity
commercial
synthetic
10 15 20 25 30 35 40 45 50 55 60 65 70 75 80
2theta/degree

Fig. 5

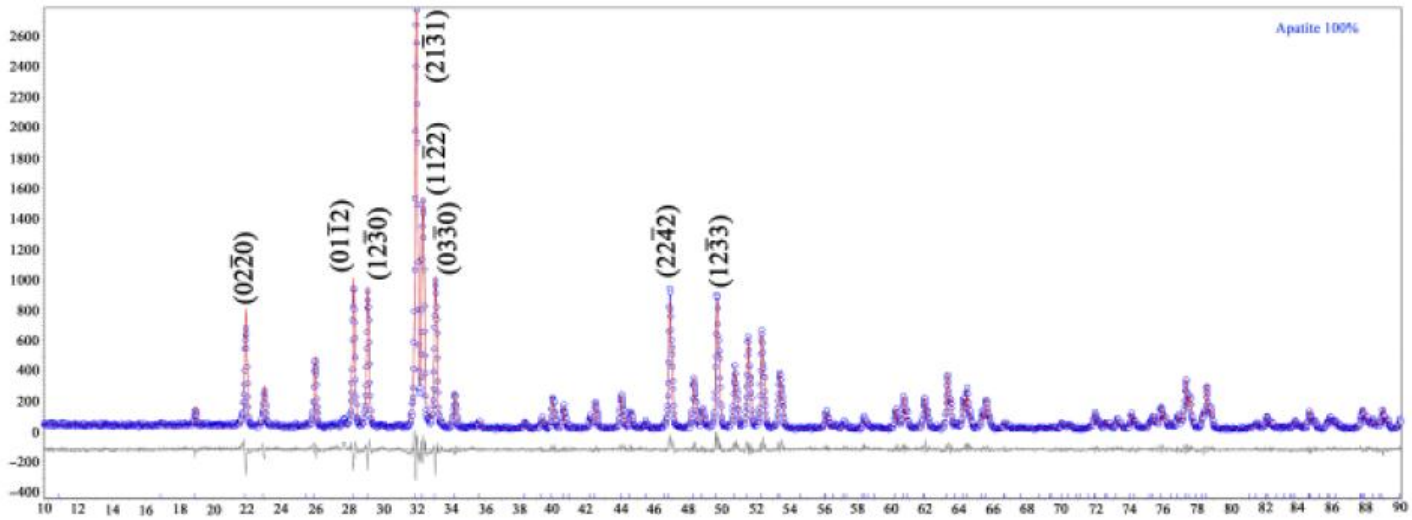
Apatite 100%
(02$\bar{2}$0)
(01$\bar{1}$2)
(12$\bar{3}$0)
(21$\bar{3}$1)
(11$\bar{2}$2)
(03$\bar{3}$0)
(22$\bar{4}$2)
(12$\bar{3}$3)

Fig. 6

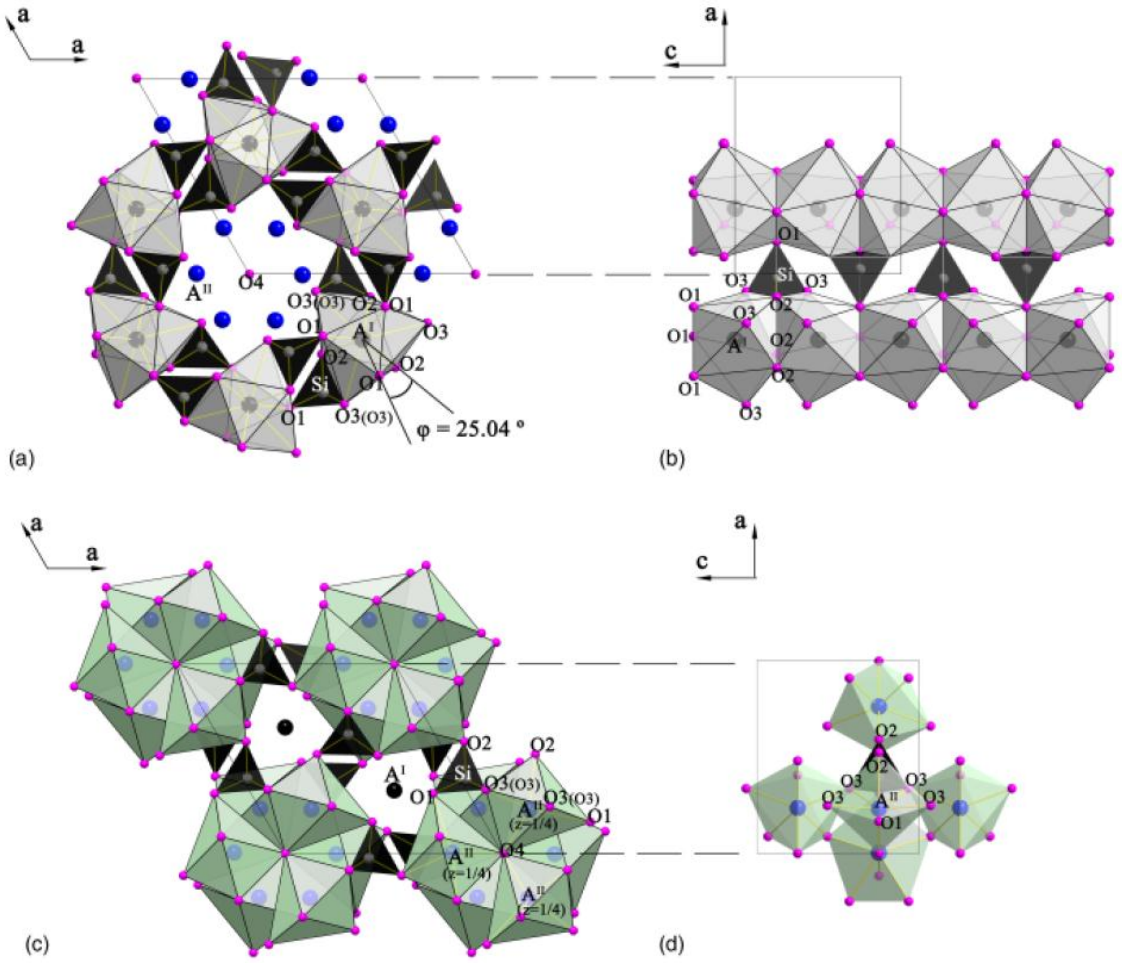
a
a
A II
O4
O3(O3)
O2
O1
O1
A I
O3
O2
Si
O2
O1
O1
O3(O3)
φ = 25.04 °
(a)
a
c
O1
Si
O3
O3
O1
O3
O2
O1
A I
O2
O1
O2
O3
(b)
a
a
O2
O2
A I
Si
O3(O3)
O1
A II
(z=1/4)
O3(O3)
O1
A II
(z=1/4)
O4
A II
(z=1/4)
(c)
a
c
O2
O2
O3
O3
A II
O3
O1
(d)

Fig. 7.

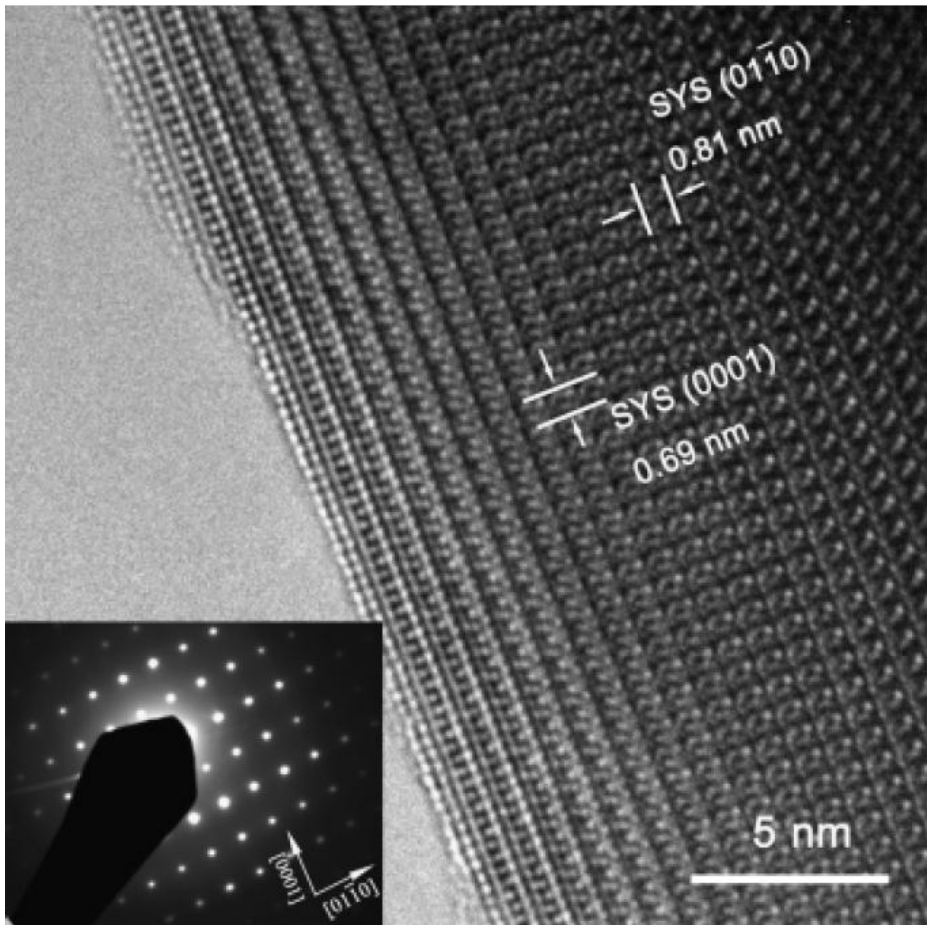

Fig. 8.